Available online at www.sciencedirect.com
SCIENCE DIRECT
Polymer Degradation and Stability 89 (2005) 353–372
Polymer Degradation and Stability
www.elsevier.com/locate/polydegstab

Modeling epoxy foams exposed to fire-like heat fluxes

Michael L. Hobbs*

Sandia National Laboratories,[1] MS-0836, PO Box 5800, Albuquerque, NM 87185-0836, United States

Received 21 October 2004; received in revised form 21 January 2005; accepted 27 January 2005
Available online 18 March 2005

Abstract

A decomposition chemistry and heat transfer model to predict the response of removable epoxy foam (REF) exposed to fire-like heat fluxes is described. The epoxy foam was created using a perfluorohexane blowing agent with a surfactant. The model includes desorption of the blowing agent and surfactant, thermal degradation of the epoxy polymer, polymer fragment transport, and vapor–liquid equilibrium. An effective thermal conductivity model describes changes in thermal conductivity with reaction extent. Pressurization is modeled assuming: (1) no strain in the condensed-phase, (2) no resistance to gas-phase transport, (3) spatially uniform stress fields, and (4) no mass loss from the system due to venting. The model has been used to predict mass loss, pressure rise, and decomposition front locations for various small-scale and large-scale experiments performed by others. The framework of the model is suitable for polymeric foams with absorbed gases.
Published by Elsevier Ltd.

Keywords: Removable epoxy foam; Decomposition; Confinement; Pressurization; Adsorbed gases

1. Introduction

Traditional encapsulants are difficult to remove due to cross-linking, solvent resistance, and mechanical toughness, and are removed for component maintenance by using aggressive solvents and/or mechanical chiseling, which can easily damage electronic assemblies. Loy et al. [1–3] recently patented a method to make thermally removable epoxy foam (REF) that can be removed from potted assemblies with a mild solvent (e.g., *n*-butanol) at 90 °C. Removability was achieved by incorporating chemically labile linkages within the cross-linked polymeric network using the reversible Diels–Alder reaction. The reverse (retro) Diels–Alder reaction is favored by heating the foamed encapsulant to temperatures near 90 °C and a mild solvent promotes dissolution of the foam.

Removable epoxy foams are used at Sandia National Laboratories to encapsulate shock and vibration sensitive components within metal enclosures. The enclosures may have cable openings that provide pathways for decomposition gases to exit the system. Conversely, some enclosures may be hermetically sealed to prevent gases from entering or exiting the system. Consequently, a decomposition model was needed with the ability to predict decomposition behavior associated with both confinement and venting of the decomposition gases as well as pressurization. This paper describes a simple removable epoxy foam (SREF) decomposition chemistry model for removable epoxy foams exposed to fire-like environments [4], where low-temperature reversible reactions, such as the Diels–Alder reaction, are considered negligible.

The model described in the current paper differs from the model in Ref. [4] by not using empirical correlations

* Tel.: +1 5058445988; fax: +1 5058448251.
E-mail address: mlhobbs@sandia.gov

[1] Sandia is a multiprogram laboratory operated by Sandia Corporation, a Lockheed Martin Company, for the United States Department of Energy's National Nuclear Security Administration under Contract DE-AC04-94AL85000.

0141-3910/$ - see front matter Published by Elsevier Ltd.
doi:10.1016/j.polymdegradstab.2005.01.021

Nomenclature

A_j	Pre-exponential factor for the jth reaction in Eq. (3), s^{-1}
a_c	Adsorptivity of the condensed-phase in Eq. (31), cm^{-1}
a_g	Adsorptivity of the gas-phase in Eq. (31), cm^{-1}
BAS	Blowing agent and surfactant
BPA	Bisphenol A
C_f	Foam specific heat in Eqs. (26) and (30), cal g^{-1} K^{-1}
$c+1$	Lattice coordination number in Eq. (11)
DGEBA	Diglycidyl ether of bisphenol A
DMDC	Dimethyldicyane
D_j	Molecular diffusivity for the jth reaction in Eqs. (7) and (8), cm^2/s
$D_{j,0}$	Molecular diffusivity for the jth reaction 298.15 K and 1 atm in Eq. (8), cm^2/s
d^*	Characteristic diffusion length in Eq. (7), cm
d^*/θ	Diffusion parameter proportional to diffusive resistance in Eq. (7), cm
E_j	Activation energy for the jth reaction in Eq. (3), cal/mol
F	Moles of VLE combined-phase species (traditionally called feed) in Eq. (17)
ϕ	Gas volume fraction in Eq. (27)
ϕ_0	Initial gas volume fraction in Eq. (27)
Φ	Cumulative distribution function of standard normal random variable in Eqs. (4) and (5)
γ_i	Activity coefficient of the ith species in Eqs. (17) and (23)
$\gamma_{i,0}$	Activity coefficient at ambient pressure in Eq. (23)
HPTGA	High-pressure thermogravimetric analysis
Δh	Change in height of load cell sample chamber in Fig. 8B, cm
K_i	Vapor–liquid equilibrium ratio in Eq. (17)
k_j	Effective rate constant for the jth reaction in Eq. (2), s^{-1}
$k_{j,c}$	Kinetic rate constant for the jth reaction in Eqs. (2) and (3), s^{-1}
$k_{j,m}$	Mass transport rate constant for the jth reaction in Eqs. (2) and (7), s^{-1}
LPTGA	Low-pressure thermogravimetric analysis
L_1	Bridge population composed of octamethylcyclotetrasiloxane in Eq. (1)
$L_{1,0}$	Initial bridge population composed of octamethylcyclotetrasiloxane in Eq. (1)
L_2	Bridge population composed of mixed products in Eq. (1)
$L_{2,0}$	Initial bridge population composed of mixed products in Eq. (1)
L_3	Bridge population composed of bisphenol A in Eq. (1)
$L_{3,0}$	Initial bridge population composed of bisphenol A in Eq. (1)
λ_c	Thermal conductivity of the condensed-phase polymer in Eq. (31), cal s^{-1} cm^{-1} K^{-1}
λ_f	Thermal conductivity of the foam in Eq. (31), cal s^{-1} cm^{-1} K^{-1}
λ_g	Thermal conductivity of the gas-phase in Eq. (31), cal s^{-1} cm^{-1} K^{-1}
MP	Mixed products
$\bar{M}_b$	Average bridge molecular weight in Eqs. (9) and (10), g/mol
$M_{c,VLE}$	Molecular weight of the condensed VLE species in Eq. (25), g/mol
$M_{g,VLE}$	Molecular weight of the gaseous VLE species in Eq. (25), g/mol
M_g	Gas molecular weight in Eq. (25), g/mol
$\bar{M}_g$	Average gas molecular weight in Eq. (28), g/mol
$\bar{M}_{g,0}$	Initial value of the average gas molecular weight at time zero in Eq. (27), g/mol
M_i	Molecular weight of population i in Table 1, g/mol
$M_{L\text{-mer}}$	Molecular weight of the L-mer fragments in Eq. (15), g/mol
M_n	Molecular weight of the n-mer in Eq. (10), g/mol
m	Sample mass used in definition of S_f, g
m_n	Mass of an n-mer on a site basis described by Eq. (11), g
m_0	Initial sample mass used in definition of S_f, g
m_t	Mass of an extended site described by Eq. (9), g
NV-residue	Nonvolatile residue
NP	Nonyl phenol
n	Number of sites in a polymer fragment used in Eq. (11)
OS	Octamethylcyclotetrasiloxane
PETA	Pentaerythritol triacrylate
P	System pressure in Eq. (29), atm
P_0	Initial system pressure in Eq. (27), atm
$P_{i,c}$	Critical pressure of the ith species in Eq. (23), atm

P^*_{BAS}	Vapor pressure of the BAS species in Eq. (18), atm
P^*_{BPA}	Vapor pressure of the BPA species in Eq. (21), atm
P^*_i	Vapor pressure of the ith species in Eq. (17), atm
P^*_{MP}	Vapor pressure of the MP species in Eq. (20), atm
P^*_{n-mer}	Vapor pressure of the n-mer species in Eq. (22), atm
P^*_{OS}	Vapor pressure of the OS species in Eq. (19), atm
p	Bridge population described by Eq. (6)
p_{BAS}	Population of blowing agent and surfactant in Table 1.
p_{OS}	Population of octamethylcyclotetrasiloxane
p_{MP}	Population of mixed products
p_{BPA}	Population of bisphenol A in Table 1
$p_{NV\text{-}residue}$	Population of nonvolatile residue in Table 1
q_j	Reaction enthalpy for jth reaction in Eq. (26), cal/g
θ	Ratio of effective diffusivity to molecular diffusivity in Eq. (7)
REF	Removable epoxy foam
REF100	Series 100 removable epoxy foam
REF200	Series 200 removable epoxy foam
REF300	Series 300 removable epoxy foam
RER1	Removable epoxy resin 1 [3]
R	Gas constant, 1.987 cal mol^{-1} K^{-1} in Eq. (3), 82.06 atm cm^3 mol^{-1} K^{-1} in Eqs. (27) and (29)
$R_{j,c}$	Chemical resistance in Eq. (2), s
$R_{j,m}$	Mass transport resistance in Eq. (2), s
r_i	Rate of reaction i in Table 1, s^{-1}
ρ_f	Bulk density of the foam in Eq. (27), g/cm^3
$\rho_{f,0}$	Initial bulk density of the foam in Eq. (27), g/cm^3
ρ_g	Gas density in Eq. (27), g/cm^3
$\rho_{p,0}$	Initial density of the polymer in Eq. (27), g/cm^3
SREF	Simple removable epoxy foam
S	"Sorbed" species population in Eq. (1)
S_0	Initial "sorbed" species population in Eq. (1)
S^*	Population of species absorbed on to the polymer at the reaction site as shown in Fig. 4
S_f	Solid fraction or normalized sample mass ($S_f = m/m_0$) in Eq. (24)
$S_{f,VLE}$	Solid fraction of the VLE species (mass of the condensed VLE species divided by the mass of the combined condensed- and gas-phase VLE species) in Eq. (17)
$S_f \times d^*$	Diffusion length in Eq. (7), cm
s	Number of bridges in a polymer fragment in Eq. (11)
σ	Stephan–Boltzmann constant used in Eq. (31), 1.3543×10^{-12} cal cm^{-2} K^{-4}
$\sigma_{E,j}$	Distributed activation energy model coefficient for the jth reaction in Eq. (3), cal/mol
TGA	Thermogravimetric analysis
T	Temperature in Eqs. (3), (8), (18)–(22), (26), (30), and (31), K
$\bar{T}_g$	Average gas temperature in Eq. (28), K
$\bar{T}_{g,0}$	Initial value of the average gas temperature at time zero in Eq. (27), K
t	Time in Eq. (26) and Fig. 1, s
t_{end}	Time at end of simulation in Fig. 1, s
τ	Number of broken bridges on the perimeter of a polymer fragment with s-bridges connecting n-sites in Eq. (11)
VLE	Vapor–liquid equilibrium
V	Moles of VLE vapor in Eq. (17)
V/F	Moles of VLE vapor divided by moles of VLE combined-phase species in Eq. (17)
V	Volume in Eq. (27), cm^3
ω_{BAS}	Mass fraction of BAS in Eq. (13)
ω_{BPA}	Mass fraction of BPA in Eq. (13)
ω_c	Mass fraction of condensed-phase in Eqs. (31) and (32)
$\omega_{NV\text{-}residue}$	Nonvolatile residue mass fraction in Eq. (14)
ω_g	Mass fraction of gas-phase in Eqs. (31) and (32)
ω_i	Mass fraction of the VLE species in Eq. (17)
$\omega_{L\text{-}mer}$	Mass fraction of the L-mers in Eq. (15)
ω_{MP}	Mass fraction of MP in Eq. (13)
$\omega_{n\text{-}mer}$	Mass fraction of the n-mers in Eq. (12)
ω_{OS}	Mass fraction of OS in Eq. (13)
$\omega_{XL\text{-}mer}$	Mass fraction of the XL-mer fragments in Eq. (16)
x	Spatial dimension in Eq. (26), cm
x_i	Mole fraction of the ith condensed-phase VLE species in Eq. (17)
y_i	Mole fraction of the ith gas-phase VLE species in Eq. (17)
z_j	Number of standard deviations for activation energy j in Eqs. (3)–(5)
z_i	Mole fraction of the ith combined-phase VLE species in Eq. (17)

to describe pressure-dependent residue formation, by not using empirical correlations to describe confinement effects, by using ideal activity coefficients at low pressures ($\gamma_i^0 = 1$), by setting unknown diffusion parameters to unity [$(d^*/\theta)_i = 1$ cm], and by changing the order of the temperature-dependent diffusivities to 1.67 instead of 1.5 to account for the temperature dependency of collision integrals, and by making the diffusivities of the blowing agents and surfactants inversely proportional to pressure. Confinement effects are investigated by increasing diffusive resistance by an order of magnitude.

The SREF decomposition model is based on the assumption that the struts and windows of the foam are composed of an epoxy polymer. The bubbles in the foam were created using a perfluorohexane blowing agent and a surfactant. Over time, the blowing agent and surfactant either *absorb* or *adsorb* on to the polymer without being intimately bonded to the polymer.[2] The epoxy polymer [1–3] was made using commercial ingredients (e.g. EPON 8121, Ancamine 2049, and EpiCure 3270) as well as a resin (RER1) produced at Sandia National Laboratories [3]. The chemical structure of the epoxy polymer, inferred from the starting materials and the synthesis method by Clayton [5], was used for the SREF model lattice.

The effects of confining the REF decomposition gases were observed by Erickson et al. [6] who studied mass loss in low-pressure thermogravimetric analysis (LPTGA) experiments using 0.4 cm diameter cylindrical sample pans with lids containing orifices with diameters ranging from 0.2 to 0.006 cm. Mass loss profiles shifted to higher temperatures as the size of the orifice decreased. Clayton [5] observed a similar shift in the mass loss profiles to higher temperatures as pressure was increased in unconfined high-pressure thermogravimetric analysis (HPTGA) experiments. Clayton [5] separated confinement effects from pressure effects by using a high-pressure helium purge gas with an open sample pan in a high-pressure reactor. The SREF model considers pressure effects by using mass transport and vapor–liquid equilibrium constraints. Confinement is addressed semi-empirically by increasing the mass transport resistance by an order of magnitude, which is equivalent to artificially decreasing the driving potential or concentration differences between species at the reaction sites and in the bulk gas. A simple flow diagram showing key parts of the decomposition model is given in Fig. 1.

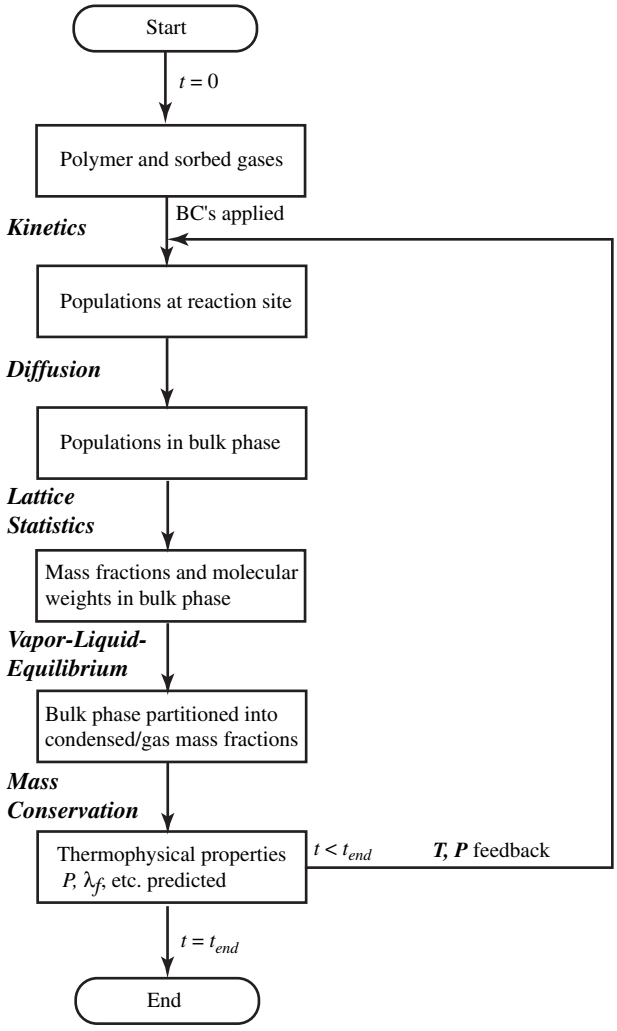

Fig. 1. Simple flow diagram showing key parts of the SREF decomposition chemistry model, where t, t_{end}, P, and λ_f represent time, time at end of simulation, pressure, and foam thermal conductivity, respectively. The term "BC" refers to the applied boundary condition.

2. Chemical structure of the REF polymer

Fig. 2A and B shows the most probable repeating unit of the REF polymer determined by Clayton [5], which is essentially an infinite network composed of various sites and bridges synthesized from the five primary ingredients shown in Fig. 2C: (1) diglycidyl ether of bisphenol A [DGEBA, $C_{21}H_{24}O_4$, 340 g/mol, 16.8 wt%], (2) ancamine 2049, which is commonly called dimethyldicyane [DMDC, $C_{15}H_{30}N_2$, 238 g/mol, 21.7 wt%], (3) a removable epoxy resin [RER1, $C_{44}H_{56}N_2O_{15}Si_4$, 964 g/mol, 42.0 wt%], (4) pentaerythritol triacrylate [PETA, $C_{14}H_{18}O_7$, 298 g/mol, 11.2 wt%], and (5) nonyl phenol [NP, $C_{15}H_{24}O$, 220 g/mol, 6.0 wt%]. A small amount of *n*-aminoethylpiperazine [*n*-AEP, $C_6H_{15}N_3$, 129 g/mol, 2.4 wt%] was also

[2] *Absorption* is the process of incorporating the blowing agent and surfactant as a part of the existent whole of the polymer. *Adsorption* refers to adhesion of an extremely thin layer of blowing agent and surfactant molecules to the surfaces of the REF polymer. *Sorbed* refers to either *absorption or adsorption*.

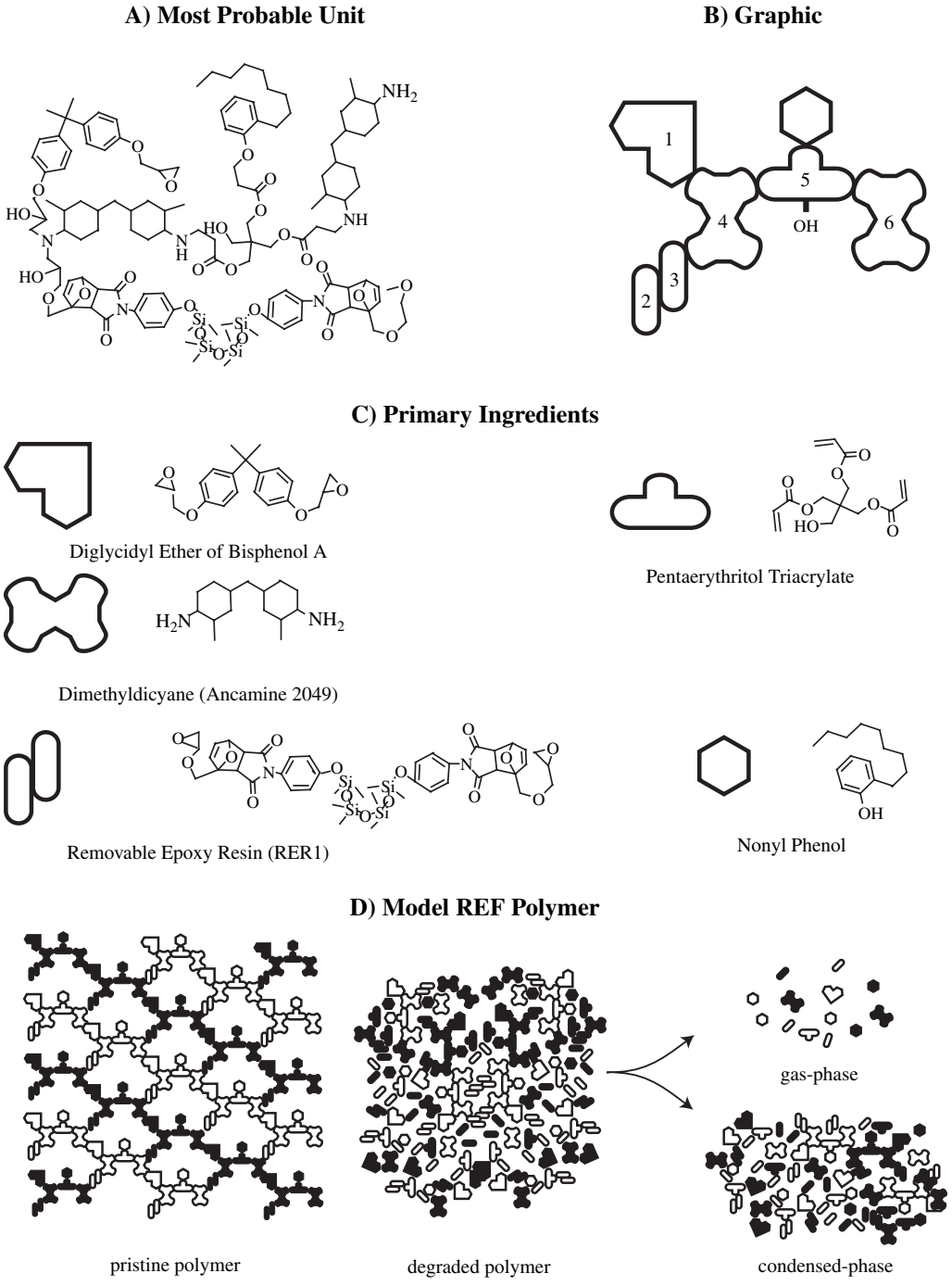

Fig. 2. (A) Most probable repeating unit, (B) graphic of most probable repeating unit, (C) primary ingredients, and (D) model of REF polymer. The graphic symbols represent ingredients used to make the polymer. The graphic in B shows six sites. The alcohol functional group on site 5 is a potential reaction site. Nonyl phenol, represented as a hexagon, is considered a terminating dangler rather than a site.

used to make the polymer. The elemental composition of the REF polymer, determined from the primary ingredients, is 64.4 wt% C, 8.0 wt% H, 4.5 wt% N, 18.2 wt% O, and 4.9 wt% Si. The foam is composed of 80.8 wt% REF polymer, 14.1 wt% perfluorohexane (C_6F_{14}), and 5.1 wt% surfactant with a proprietary composition.

Fig. 2B shows a simple graphic of the most probable structural unit with six potential lattice sites. A site is a point from which a lattice or network can be propagated, by connecting to other sites as discussed in more detail in Section 5. Each of the graphic shapes corresponds to part of the polymer, which can propagate via reactive functional groups. For example,

site 5, associated with PETA in Fig. 2B, has four potentially reactive groups – three of the acrylate functional groups have already reacted and the hydroxyl group (–OH) can potentially react. Sites 1, 2, 3, 4, 5, and 6 have respective coordination numbers 2, 2, 2, 4, 4, and 4, which make the average coordination number of the REF polymer 3. The average coordination number is the numerical average of the six sites labeled "1" through "6" in Fig. 2B, which is a simple graphic representation of the most probable unit shown in Fig. 2A.

In Fig. 2B, the hexagonal graphic figure representing nonyl phenol is not considered a site since there are no lattice-propagating reactive groups associated with this moiety. The only reactive group on the nonyl phenol is the hydroxyl group, –OH. The hydroxyl group can react with other functional groups such as the acrylate groups associated with PETA or hydrogen associated with the $-NH_2$ functional groups. Once the nonyl phenol's hydroxyl group reacts, no other functional groups are available to continue the chain propagation.

Fig. 2D also shows a model REF polymer composed of the most probable structural unit shown in black and white. In Fig. 2D, the removable epoxy resin (RER1) is shown connecting the white polymer sections to the black polymer sections. As the temperature is increased, these sections separate and cause the polymer to unzip. Of course the representative polymer in Fig. 2D is more orderly than would be expected in the actual polymer network, and the unzipping would create various polymer fragments that are soluble in mild solvents. When exposed to fire-like heat fluxes, the polymer will decompose and create polymer fragments that behave like solvent molecules that promote liquefaction. As shown in Fig. 2D, the decomposition products separate into the gas-phase, condensed-phase, or mixed-phase depending on the system pressure and the vapor pressure of the various polymer fragments.

3. Kinetics

3.1. Observations

Fig. 3 shows a typical mass loss profile plotted as the normalized sample mass or solid fraction ($S_F = m/m_0$) for an initial 5-mg sample heated from room temperature at 20 °C/min [5]. Fig. 3 also shows the rate of mass loss divided by the heating rate ($-dS_f/dT$). The four peaks labeled A–D in Fig. 3 indicate multiple, temperature-dependent reaction steps. Erickson et al. [6] have monitored the decomposition gases from the TGA using real-time FTIR and have periodically analyzed gas samples using a gas chromatograph and mass spectrometer. From room temperature to about 140 °C, the most abundant decomposition products were the blowing agent (perfluorohexane, C_6F_{14}, b.p. 58–60 °C) and siloxanes associated with the surfactant, which correspond to peak A in Fig. 3. From about 140 to 300 °C, the major decomposition product is octamethylcyclotetrasiloxane (OS, b.p. 175–176 °C), corresponding to peak B in Fig. 3. The OS peak (B) was not observed for the partially confined experiments using small orifice sizes [6]. Peaks C and D are associated with a mixture of organic products that include 2-methylfuran, phenol, toluene, nonyl phenol (NP), and bisphenol A (BPA). Less volatile products such as BPA are more prevalent in the fourth peak labeled D in Fig. 3.

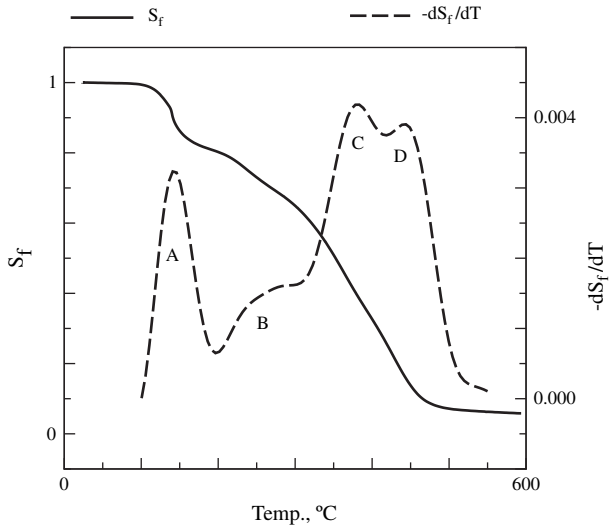

Fig. 3. TGA mass loss and rate of mass loss from an unconfined 4.7 mg REF sample heated at 20 °C/min [5]. A–D show four primary decomposition steps.

3.2. Mechanism

At least four reactions are needed to reproduce the mass loss profiles shown in Fig. 3. Reversible reactions were not included in the mechanism since the model application is for foam exposed to hydrocarbon fuel fires where reversible reactions are believed to be inconsequential. For example, the Diels–Alder reaction goes in the forward direction at 60 °C and reverses at or above 90 °C [3]. These low temperatures are rapidly surpassed in fire environments where heating rates and temperatures are high. The four-step SREF reaction mechanism is given in Table 1 along with rate equations, populations, molecular weights, and initial compositions for three REF formulations. REF100 refers to the foam described in Ref. [3]. Two additional formulations, REF200 and REF300, were developed to insure that the glass transition temperature would be well above normal operating temperatures. Kinetic parameters for REF100, REF200, and REF300 are assumed to be the same.

In Table 1, the mass-based populations, S, L_1, L_2, and L_3, represent the blowing agent and surfactant

Table 1
Mechanism, rate equations, and initial conditions for the SREF model

Reactions	Mechanism	Rate equations	Populations	M (g/mol)	Initial composition		
					REF100	REF200	REF300
1	$S \xrightarrow{1} p_{BAS}$	$r_1 = k_1 S$	S	120[a]	0.192	0.150	0.130
2	$L_1 \xrightarrow{2} p_{OS}$	$r_2 = k_2 L_1$	L_1	296	0.104	0.104	0.104
3	$L_2 \xrightarrow{3} p_{MP}$	$r_3 = k_3 L_2$	L_2	140[b]	0.563	0.537	0.589
4	$L_3 \xrightarrow{4} p_{BPA}$	$r_4 = k_4 L_3$	L_3	228	0.091	0.091	0.091
			$p_{NV\text{-residue}}$	1000[c]	0.050	0.118	0.086

[a] M estimated from blowing agent (C_6F_{14}, 338 g/mol) and surfactant of unknown molecular weight.
[b] M estimated from mixed products such as furans, phenols, cresols.
[c] M estimate for large molecular weight residues.

(BAS) that are *sorbed* onto the polymer, the labile bridges composed of octamethylcyclotetrasiloxane (OS), the labile bridges composed of mixed products (MP), and the labile bridges composed of bisphenol A (BPA), respectively. In Table 1, p_{BAS}, p_{OS}, p_{MP}, and p_{BPA} are also mass-based population variables; and rate equations can also be written for each of these variables. However, these populations can be obtained using conservation of mass since there are no reversible reactions in the SREF mechanism:

$$p_{BAS} = S_0 - S,\ p_{OS} = L_{1,0} - L_1,\ p_{MP} = L_{2,0} - L_2, \text{ and } p_{BPA} = L_{3,0} - L_3, \quad (1)$$

where $S_0, L_{1,0}, L_{2,0},$ and $L_{3,0}$ represent the initial mass fraction of the "sorbed" blowing agent and surfactant, the portion of the removable resin (RER1) that decomposes as octamethylcyclotetrasiloxane at high temperatures, the portion of the polymer that evolves as a variety of mixed products at high temperatures, and the portion of the polymer that decomposes into bisphenol A at elevated temperatures.

3.3. Initial conditions

The initial compositions listed in Table 1 are mass fractions obtained from the initial foam constituents as discussed in Ref. [4]. In Table 1, the nonvolatile residue (NV-residue), estimated from TGA experiments such as shown in Fig. 3, is composed of carbon, hydrogen, nitrogen, oxygen, and/or silicon. NV-residue represents portions of the initial polymer structure that do not vaporize at typical fire temperatures. NV-residue may be composed of strongly cross-linked portions of the polymer or inorganic constitutives. For example, Ref. [7] describes removable syntactic foam that uses glass micro balloons in lieu of blowing agent. For such foams, the NV-residue would include the mass of silicon oxide associated with the micro balloons. In coals, NV-residue would also include mineral matter that eventually forms ash. The amount of NV-residue depends on the specific polymer and is different for REF100, REF200, and REF300. The *final condensed mass fraction* is a function of the heating conditions, pressurization, and the extent of confinement and is always greater than or equal to the NV-residue.

3.4. Chemical rate constants

The rate constants given in Table 1 are effective rate constants:

$$k_j = \left(1/k_{j,c} + 1/k_{j,m}\right)^{-1} = \left(R_{j,c} + R_{j,m}\right)^{-1}, \quad (2)$$

where $k_{j,c}$, $k_{j,m}$, $R_{j,c}$, and $R_{j,m}$ represent chemical kinetic rate constants, mass transport rate constants, chemical kinetic resistance, and mass transport resistance, respectively. Eq. (2) is used to determine the formation rate of decomposition products, not the phase (vapor–liquid split) of the decomposition products or flow of decomposition products into or out of the system of interest. The phase of the decomposition products is determined by assuming vapor–liquid equilibrium as discussed further in Section 6. Gas flow maintains pressure equilibrium between the system and the surroundings in open systems. The system pressure can be set equal to the surrounding pressure if the system vent area is large. If the vent area is small, the system pressure is determined using the difference between gas formation rates and gas flow rate out of the system using either sonic or subsonic flow equations. In closed systems, gas formation causes the system pressure to increase as discussed further in Section 7.

Eq. (2) was derived assuming that the chemical reaction rates are proportional to the site concentration, e.g. $r_{1,c} = k_{1,c} S^*$, and the diffusion rate is proportional to concentration differences, e.g. $r_{1,d} = k_{1,d}(S^* - S)$. Fig. 4 shows the sorbed gas concentration at the reaction site and a potential diffusion path to the bulk gas. By setting the diffusion rate equal to the chemical reaction rate, e.g. $r_{1,d} = r_{1,c}$, the unknown concentration of S^* can be eliminated to give an effective rate that is proportional to S, e.g. $r_1 = \left[1/\left(1/k_{1,c} + 1/k_{1,m}\right)\right] S$. A similar analysis can be done for the polymer fragments associated with OS, MP, and BPA.

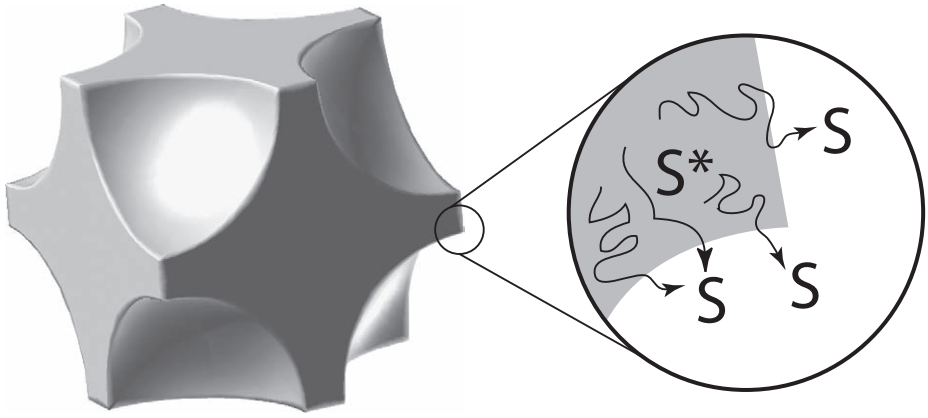

Fig. 4. Unit foam cell showing the "sorbed" species at the reaction site and a potential diffusion path to the bulk gas within a bubble.

The kinetic rate constants, $k_{1,c}$, are composed of distributed activation energies. Pitt [8] first used distributed activation energies with a simple reaction to approximate decomposition of coal as a many component mixture that decomposed independently. Distributing the activation energy smoothes the reaction rates and eliminates abrupt changes in calculated solid fractions. The four SREF reactions were distributed normally with respect to reaction extent to approximate the effect of thermal damage such as cracks, fissures, density changes, phase change, and chemical change caused by thermal decomposition.

The kinetic constant using distributed activation energies is

$$k_{j,c} = A_j \exp\left[-\left(E_j + z_j \sigma_{E,j}\right)/\mathrm{R}T\right], \tag{3}$$

where A represents the pre-exponential factors (1×10^{13}, 2×10^{15}, 2×10^{16}, and 6×10^{12}, for reactions 1, 2, 3, and 4, respectively. E represents the mean activation energies (28.7, 46.4, 58.1, and 43.5 kcal/mol for reactions 1, 2, 3, and 4, respectively). $\sigma_{E,j}$ represents the standard deviation parameter for the jth reaction used with the distributed activation energy model (0.76, 2.8, 6.6, and 0.79 kcal/mol for reactions 1, 2, 3, and 4, respectively). z, R, and T are the ordinate of the cumulative distribution factor (Φ), gas constant, and temperature, respectively. The subscript j refers to reactions 1–4 in Table 1. For the desorption reaction (reaction 1 in Table 1), the activation energy was distributed based on the extent of reaction 1 as follows:

$$\Phi = 1 - S/S_0 = \int_{-\infty}^{z} \frac{1}{\sqrt{2\pi}} \exp\left(-\frac{1}{2}z^2\right) \mathrm{d}z. \tag{4}$$

$1 - S/S_0$ and z represent the extent of the BAS desorption reaction and the ordinate of the cumulative distribution function representing the number of standard deviations above or below the mean activation energy, respectively. The polymer degradation reactions (reactions 2–4 in Table 1) were distributed based on the extent of bridge breaking as follows:

$$\Phi = 1 - p = \int_{-\infty}^{z} \frac{1}{\sqrt{2\pi}} \exp\left(-\frac{1}{2}z^2\right) \mathrm{d}z, \tag{5}$$

where p is the normalized bridge population:

$$p = (L_1 + L_2 + L_3)/(1 - S_0). \tag{6}$$

The factor $(1 - S_0)$ converts from a foam basis that includes BAS to a polymer basis with no BAS.

4. Mass transport rate constants

The mass transport rate constant can be written in terms of the effective diffusivity, θD_j, and diffusion length, $S_\mathrm{f} d^*$, as follows [4]:

$$k_{j,\mathrm{m}} = \frac{2\theta D_j}{S_\mathrm{f} d^*}, \tag{7}$$

where D_j and S_f are the gas-phase molecular diffusivity and the reacted solid fraction, respectively. "d^*" is a characteristic diffusion length. In Eq. (7), "2" is the limiting value of the Sherwood number for mass transfer from spheres at low Reynolds numbers. The product $S_\mathrm{f} \times d^*$ forces the diffusion resistance ($1/k_{j,\mathrm{m}}$) to behave correctly in the limit as the condensed mass approaches zero. As the reacted solid fraction goes to zero, the mass transport resistance ($1/k_{j,\mathrm{m}}$) also goes to zero. θ is the ratio of the true diffusivity to the gas-phase diffusivity and is based on the developing porosity of the degraded foam as discussed by Laurendeau [9]. Froment and Bishoff [10] also describe diffusion in porous catalysts using the same form for effective diffusivity, θD_j.

The four molecular diffusivities used to determine the four mass transport rate constants in Eq. (7) were

assumed to have the following temperature and pressure dependency:

$$D_1 = D_{1,0}\left(\frac{T}{298.15}\right)^{1.67} P^{-1},\ D_2 = D_{2,0}\left(\frac{T}{298.15}\right)^{1.67},$$
$$D_3 = D_{3,0}\left(\frac{T}{298.15}\right)^{1.67},\ \text{and}\ D_4 = D_{4,0}\left(\frac{T}{298.15}\right)^{1.67}, \quad (8)$$

where $D_{1,0} = 0.0067\ \text{cm}^2/\text{s}$, $D_{2,0} = 0.0062\ \text{cm}^2/\text{s}$, $D_{3,0} = 0.021\ \text{cm}^2/\text{s}$, and $D_{4,0} = 0.0073\ \text{cm}^2/\text{s}$ represent the initial mass diffusivities at 298 K and 1 atm for reactions 1, 2, 3, and 4, respectively. The initial diffusivities were estimated using Chapman–Enskog theory [11] for reactions 1–4 with critical properties of the blowing agent, OS, phenol, and BPA, respectively, as discussed further by Hobbs [4]. The polymer fragment diffusivities are assumed to be independent of pressure, which is consistent with theoretical and empirical liquid diffusivity correlations [11].

The characteristic diffusion length, d^*, and the ratio of the effective diffusivity to the molecular diffusivity, θ, are unknown parameters in Eq. (7). d^* is related to the average distance from the reaction site to the bulk gases which accumulate in bubbles, and θ is related to the porosity and tortuosity of the degraded material. Reaction products either diffuse directly to the surface of the foam polymer or to nearby bubbles that are convectively transported to the foam polymer surface. Diffusion to a bubble is assumed to be slower than convective bubble transport. These unknown diffusion parameters are approximated together as d^*/θ and the value for all four reactions is assumed to be 1 cm in the current paper. A few simulations are performed with d^*/θ increased by an order of magnitude to qualitatively investigate confinement effects.

5. Lattice statistics

Hobbs et al. [12] have used percolation theory following Grant et al. [13,14] to describe thermal decomposition of polymeric foams by relating postulated chemical structures to "tree-like" Bethe lattice networks composed of sites connected by bridges. The REF polymer lattice was approximated with Bethe lattices to determine the distribution of various polymer fragments. A polymer fragment containing n-sites is referred to as an n-mer. Polymer fragments containing 1, 2, 3, or an infinite number of sites are referred to as a monomer (or 1-mer), a dimer (or 2-mer), a trimer (or 3-mer), or an infinite-mer (or ∞-mer), respectively.

Fig. 5A shows the most common chemical structural unit for the REF polymer with the pentaerythritol triacrylate (PETA) site highlighted. A detailed schematic of the "extended PETA site" is shown in Fig. 5B. A simpler "extended PETA site", used in the SREF lattice

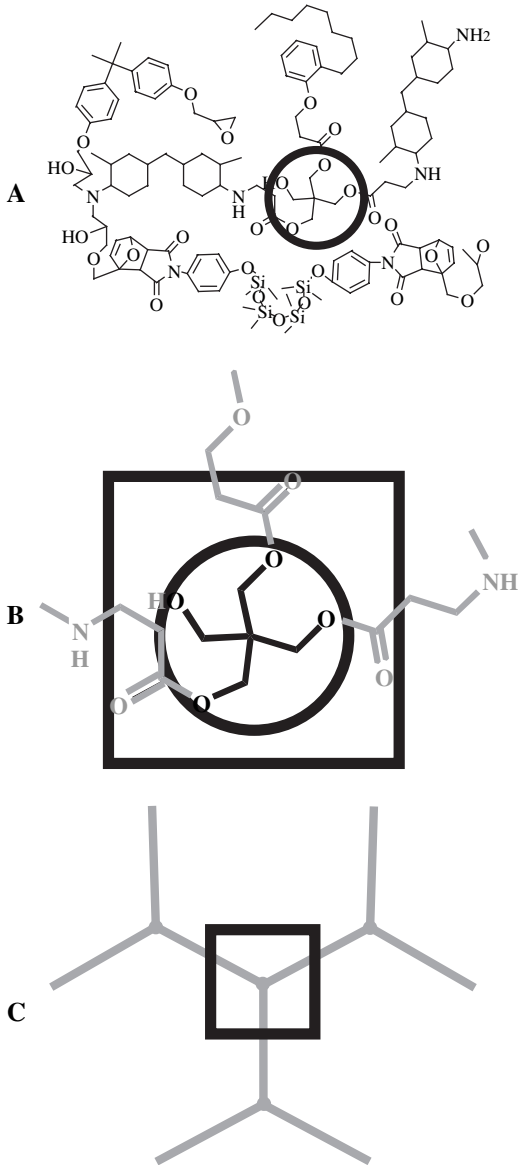

Fig. 5. (A) Most common chemical structural unit with pentaerythritol triacrylate (PETA) site highlighted, (B) detailed "extended site" in black square, and (C) simple "extended site" in black square used in SREF model. In part B, the "site" contains atoms that are colored black. The atoms associated with the bridges connecting other sites are colored gray. The "extended site" includes the black site atoms and half of the gray bridge atoms from neighboring extended sites. In part C, there are no atoms associated with the "site." The "extended site " in part C is only composed of bridge atoms.

statistics model, is shown in Fig. 5C. The mass of the extended site, m_t, is based on the average molecular weight of the bridges connecting the sites, $\overline{M}_b$, as follows:

$$m_t = \frac{3}{2}\overline{M}_b. \quad (9)$$

The factor 3/2 represents three of the half bridges enclosed within the black square in Fig. 5C.

The average molecular weight of the bridges connecting sites, $\overline{M}_b = 172$ g/mol, was determined from the initial bridge populations and bridge molecular weights [4]. The simple lattice in Fig. 5C does not associate mass with the sites; and the entire polymer mass is assumed to be located in the bridges. In other words, the extended site for the SREF model only contains mass associated with bridges. Furthermore, bridges are assumed to be either occupied or unoccupied, implying that *monomers defined in the current paper do not have mass*. The molecular weight of an n-mer is the sum of the bridges connecting sites:

$$M_n = (n-1)\overline{M}_b, \tag{10}$$

where the average bridge molecular weight is 172 g/mol.

The mass of an n-mer on a site basis can be obtained by multiplying the n-mer molecular weight in Eq. (10) by the number density of the n-site fragments on a per site basis:

$$m_n = \frac{(n-1)\overline{M}_b}{n}\left[\frac{c+1}{\tau+s}\binom{\tau+s}{n-1}p^s(1-p)^\tau\right], \quad \text{where } \tau = n(s-1)+2 \text{ and } s = n-1 \tag{11}$$

as discussed in detail by Hobbs [4]. τ is the number of broken bridges on the perimeter of the n-mer with s-bridges connecting n-sites. The factor $(c+1)/(\tau+s)$ converts from a bridge basis to a site basis. The binomial expression,

$$\binom{\tau+s}{n-1},$$

represents the number of distinct n-mer configurations that can be obtained from $\tau + s$ potential bridges. $c+1$ is the coordination number of the polymer which is 3, as discussed in Section 2. The mass fraction of n-mers can be determined by the ratio of the n-mer mass *on a site basis* in Eq. (11) to the site mass in Eq. (9):

$$\omega_{n\text{-mer}} = \frac{m_n}{m_t}(1 - S_0). \tag{12}$$

The factor $(1 - S_0)$ converts the mass fraction to a foam basis that includes BAS rather than a polymer basis that does not include BAS.

The mass fractions of the BAS, OS, MP, and BPA species, ω_{BAS}, ω_{OS}, ω_{MP}, and ω_{BPA}, can be determined directly from the population variables calculated using Eq. (1) since these progress variables track the reaction in terms of mass fractions. The mass fractions of BAS, OS, MP, and BPA are:

$$\omega_{BAS} = p_{BAS}, \omega_{OS} = p_{OS}, \omega_{MP} = p_{MP,} \text{ and } \omega_{BPA} = p_{BPA}, \tag{13}$$

where the molecular weights of BAS, OS, MP, and BPA are taken to be 120, 296, 140, and 228 g/mol, respectively, and are given in Table 1. The mass fractions of the NV-residue are constant as given in Table 3:

$$\omega_{NVresidue,REF100} = 0.05,\ \omega_{NV\text{-}residue,REF200} = 0.118, \text{ and } \omega_{NV\text{-}residue,REF300} = 0.086. \tag{14}$$

The molecular weights of the NV-residue were assumed to be 1000 g/mol.

The SREF model formally considers 10 species – (1) BAS, (2) OS, (3) MP, (4) BPA, (5) 2-mers, (6) 3-mers, (7) 4-mers, (8) NV-residue, (9) L-mers, and (10) XL-mers. The mass fractions for the first eight species can be determined by Eqs. (12)–(14). The L-mer population represents the n-mer ranging from the 5-mer population up to max-mer population. The max-mer should be less than 500 to prevent computer overflow errors, although a value of 10 gives essentially the same results as 500 and was used for the calculations in the current paper. The mass fraction and molecular weight of the L-mer population are calculated as follows:

$$\omega_{L\text{-mer}} = \sum_{n=5}^{max}\omega_{n\text{-mer}} \text{ and } M_{L\text{-mer}} = 1/\sum_{n=5}^{max}\frac{\omega_{n\text{-mer}}}{\omega_{L\text{-mer}}(n-1)\overline{M}_b}. \tag{15}$$

The XL-mer population represents the n-mers that range from the max-mer population to the ∞-mer populations. The mass fractions of the XL-mer populations were determined using continuity constraints:

$$\omega_{XL\text{-mer}} = 1 - \omega_{BAS} - \omega_{OS} - \omega_{MP} - \omega_{BPA} - \sum_{2}^{max}\omega_{n\text{-mer}} - \omega_{NV\text{-residue}}. \tag{16}$$

The molecular weight of the XL-mer population was assumed to be 4000 g/mol.

6. Vapor–liquid equilibrium (VLE)

The previous section provided a method to calculate the mass fractions and molecular weights of 10 decomposition species. Seven of these species – (1) BAS, (2) OS, (3) MP, (4) BPA, (5) 2-mers, (6) 3-mers, (7) 4-mers – are referred to as "VLE species" since vapor–liquid equilibrium is used to partition these species into the condensed-phase, the gas-phase, or both phases. The remaining three species—(8) NV-residue, (9) L-mers, and (10) XL-mers—are referred to as "non-VLE species" since they have extremely large molecular weights and are

assumed to remain in the condensed-phase. The fraction of the VLE species in the condensed-phase, $S_{f,VLE}$, was determined using a standard multicomponent flash calculation based on the Rachford–Rice equation [15]:

$$0=\sum_{i=1}^{7}\frac{z_i(K_i-1)}{(K_i-1)\frac{V}{F}+1},\ K_i=\frac{\gamma_i P_i^*}{P},\ x_i=\frac{z_i}{(K_i-1)\frac{V}{F}+1},$$
$$y_i=K_i x_i,\ z_i=\left(\frac{\omega_i}{M_i}\right)\Big/\sum_{i=1}^{7}(\omega_i/M_i),\ \text{and}$$
$$S_{f,VLE}=\sum_{i=1}^{7}\left[x_i M_i\left(1-\frac{V}{F}\right)\right]\Big/$$
$$\left\{\sum_{i=1}^{7}\left[x_i M_i\left(1-\frac{V}{F}\right)\right]+\sum_{i=1}^{7}\left[y_i M_i\left(\frac{V}{F}\right)\right]\right\}. \quad (17)$$

z_i is the combined-phase mole fraction determined from the combined-phase mass fractions (ω_i) and molecular weights (M_i) of the ith VLE species. x_i and y_i are the condensed-phase and vapor-phase mole fractions of the ith VLE species, respectively. K_i is the vapor–liquid equilibrium ratio or K-value of the ith VLE species. The ratio, V/F, is determined iteratively and represents the total moles in the vapor-phase divided by the total moles in the combined vapor and condensed-phases. γ_i is the activity coefficient of the ith VLE species; P_i^* is the vapor pressure of the pure component at the system temperature; and P is the system pressure.

The vapor pressures of the seven VLE species were determined from [4]:

$$P_{BAS}^*=38\,900\times10^{-1560/T}+10\,700\times10^{-1950/T}, \quad (18)$$

$$P_{OS}^*=9.87\times10^{-6}\exp\left(19.4-75\,000T^{-1.5}\right), \quad (19)$$

$$P_{MP}^*=9.87\times10^{-6}\exp\left(59-\frac{8050}{T}-4.9\ln T+0.00028T\right), \quad (20)$$

$$P_{BPA}^*=9.87\times10^{-6}\exp\left(401-\frac{33\,800}{T}-55\ln T+0.028T\right), \quad (21)$$

$$P_{n\text{-mer}}^*=8.71\times10^{4}\exp\left[-300(M_n)^{0.6}/T\right], \quad (22)$$

where vapor pressure, P_i^*, is in atm and the temperature, T, is in K. The molecular weights of the 2-mer, 3-mer and 4-mer (M_n) are 172, 344, and 516 g/mol, respectively, as determined by Eq. (10). The vapor pressure for the mixed-product (MP) species is assumed to be the same as phenol.

The activity coefficients were chosen to limit the influence of pressure above critical conditions using the following equation:

$$\gamma_i=\begin{cases}\gamma_{i,0} & \text{if } P\le P_{i,c}\\ \gamma_{i,0}\frac{P}{P_{i,c}} & \text{if } P>P_{i,c}\end{cases} \quad (23)$$

where the ideal activity coefficient, $\gamma_{i,0}=1$. The effect of the SREF activity coefficient model is to prevent the separation factor from approaching zero as the thermodynamic pressure exceeds the critical pressure. $P_{i,c}$ represents the critical pressure of the ith species. The critical pressures for BAS, OS, MP, BPA, 2-mers, 3-mers, and 4-mers were chosen to be 5, 13.1 [16], 52 [16], 28.9 [16], 40, 40, and 40 atm, respectively. The critical pressures of BAS and the polymer fragments were estimated. The critical pressures for the mixed-product (MP) gases were assumed to be the average critical pressure of various cresols, phenols and furans.

The condensed-phase VLE species were then combined with the non-VLE species and the molecular weights of both phases were determined. The solid fraction is determined by adding the condensed VLE species to the non-VLE species:

$$S_f=\omega_{NV\text{-residue}}+\omega_{L\text{-mer}}+\omega_{XL\text{-mer}}+S_{f,VLE}\times(1-\omega_{NV\text{-residue}}-\omega_{L\text{-mer}}-\omega_{XL\text{-mer}}), \quad (24)$$

where $S_{f,VLE}$ is the mass fraction of the condensed-phase VLE species determined by Eq. (17). The molecular weight of the condensed VLE species ($M_{c,VLE}$) and vapor VLE species ($M_{g,VLE}$) are:

$$M_{c,VLE}=\sum_{i=1}^{7}x_i M_i \text{ and } M_{g,VLE}=M_g=\sum_{i=1}^{7}y_i M_i. \quad (25)$$

The molecular weight of the gas-phase (M_g), is the same as the molecular weight of the gas-phase VLE species and is used in the pressure calculation discussed further in Section 7.

7. Finite element implementation with pressurization

The SREF decomposition model was implemented into a finite element heat transfer model. Pressurization was determined assuming zero thermal or mechanical strain in the condensed-phase, negligible flow resistance in the gas-phase, spatially uniform stress fields, and no mass loss from the system due to venting. Spatially uniform stress fields arise when velocities are significantly less than sound speeds as discussed by Paolucci

[17]. The finite element model solves the heat diffusion equation with a source term for chemistry:

$$\rho_f C_f \frac{\partial T}{\partial t} = \frac{\partial}{\partial x}\left(\lambda_f \frac{\partial T}{\partial x}\right) + \sum_{j=1}^{4} q_j r_j. \tag{26}$$

where T is the temperature of both the gas- and condensed-phases. The reaction enthalpies determined by Hobbs [4] using differential scanning calorimeter data from Erickson [18], q_j, are -61, -11, -101, and $+82$ cal/g for reactions 1, 2, 3, and 4, respectively. The species equations, $dS/dt = r_1$, $dL_1/dt = r_2$, $dL_2/dt = r_3$, and $dL_3/dt = r_4$ are solved at each integration or Gauss point in the finite element model. Temperature is determined at the node points. The four reaction rates are listed in Table 1. The density, specific heat, and thermal conductivity of the foam are represented by ρ_f, C_f, λ_f, respectively.

The foam density, ρ_f, the gas volume fraction, ϕ, and gas density ρ_g are:

$$\rho_f = \phi\rho_g + (1-\phi)\rho_{p,0},\ \phi = 1 - S_f\left(\rho_{f,0}/\rho_{p,0}\right),\ \text{and}$$
$$\rho_g = \frac{\frac{P_0 \int_V \phi_0\, dV}{\overline{M}_{g,0} R \overline{T}_{g,0}} + \int_V (1\text{-}S_f)\rho_{f,0}\, dV}{\int_V \phi\, dV}. \tag{27}$$

The polymer density, $\rho_{p,0}$, is assumed to be constant throughout the reaction progress since no thermal or mechanical strain is allowed in the condensed-phase. The gas density was determined by dividing the mass of the gas in the system by the gas volume in the system. The mass of the gas includes the initial gas in the foam as well as decomposition gas products. The initial gas mass is determined using the ideal gas law with the initial pressure, P_0, initial gas volume fraction, ϕ_0, the initial average gas molecular weight, $\overline{M}_{g,0}$, and the initial average gas temperature, $\overline{T}_{g,0}$. The initial gas was assumed to be BAS.

The change in internal energy for a closed system is constant. For this situation, the energy average gas temperature within the permeable regions of the foam and the volume average gas molecular weight are:

$$\overline{T}_g = \frac{\int_V \rho_f C_f T\, dV}{\int_V \rho_f C_f\, dV} \text{ and } \overline{M}_g = \frac{\int_V M_g\, dV}{\int_V dV}. \tag{28}$$

The system pressure can be determined with the ideal gas law, the density from Eq. (27), the average gas temperature and molecular weight from Eq. (28) to give

$$P = \frac{\rho_g R \overline{T}_g}{\overline{M}_g}. \tag{29}$$

The specific heat was measured by various investigators [21–23] and varies linear up to the glass transition temperature, 70 °C. Above the glass transition temperature, the specific heat, C_f, was assumed to be constant:

$$C_f = \begin{cases} 0.0011T + 0.33535\ \text{cal g}^{-1}\text{K}^{-1} & T < 343.15\ \text{K} \\ 0.411\ \text{cal g}^{-1}\text{K}^{-1} & T \geq 343.15\ \text{K} \end{cases}, \tag{30}$$

where T is in K.

The thermal conductivity of the foam, λ_f, was assumed to be composed of contributions from the gas-phase, $\phi\lambda_g$, and solid phase $(2/3)(1-\phi)\lambda_c$, and radiation $\left(16\sigma/3\left(\omega_g a_g + \omega_c a_c\right)\right)T^3$:

$$\lambda_f = \phi\lambda_g + \frac{2}{3}(1-\phi)\lambda_c + \frac{16\sigma}{3\left(\omega_g a_g + \omega_c a_c\right)}T^3,$$
$$\lambda_g = \frac{-5.59T^{0.557}}{1 - 1.384\times 10^9/T}, \text{ and}$$
$$\lambda_c = 4.37\times 10^{-4}\text{cal s}^{-1}\text{cm}^{-1}\text{K}^{-1}. \tag{31}$$

λ_f, λ_g, λ_c are the thermal conductivities of the foam, decomposition gases, and polymer in cal s^{-1} cm^{-1} K^{-1}, respectively. σ is the Stephan–Boltzmann constant, 1.3543×10^{-12} cal cm^{-2} K^{-4}. T is the temperature in K. The gas thermal conductivity (λ_g) is assumed to be the same as phenol [4,16]. The "2/3" factor in Eq. (31) represents a tortuosity term. For example, if the gas defects were rectangular with six sides, only four sides would contribute to condensed-phase conductive heat transport ((4 sides/6 sides) = 2/3) for a given direction as discussed further by Glicksman [19]. The radiation contribution to the effective thermal conductivity model assumes Rosseland diffusion with the extinction coefficient separated into vapor- and condensed-phase contributions [19]. Collishaw and Evans [20] review various effective thermal conductivity models.

In Eq. (31), ω_g and ω_c are the mass fractions of gas- and condensed-phases, respectively:

$$\omega_g = \phi\rho_g / \left[(1-\phi)\rho_{p,0} + \phi\rho_g\right] \text{ and } \omega_c = 1 - \omega_g. \tag{32}$$

In Eq. (31), the adsorptivity of the gas- and condensed-phases are represented by a_g and a_c, which are taken to be constant at values of 0.1 and 0.2 cm^{-1}, respectively.

8. Small-scale predictions

Two types of small-scale experiments were simulated: (1) ramped and isothermal TGA experiments and (2) a constant volume hot cell experiment. The temperature of the foam in both of these small-scale experiments was specified and a solution of the energy equation, Eq. (26), was not required. The energy equation is solved for the larger-scale predictions in Section 9. Pressure was

specified for the TGA experiments. Pressure was calculated by Eq. (29) for the constant volume hot cell experiment.

Table 2 gives the primary SREF model parameters. A mean value method [24] was used to determine uncertainty in the predicted solid fractions for the TGA simulations and in the predicted pressure in the constant volume hot cell experiment. A 95% prediction uncertainty was determined by assuming that the activation energies are independent random variables and that the response is linear. Only the four activation energies were used to determine the uncertainty interval in this section since activation energies were shown to be the primary parameters that affect the uncertainty in model response in Ref. [4].

8.1. Ramped and isothermal TGA

Fig. 6A–D shows various predictions and measurements [6] for a *ramped TGA experiment* where the temperature of a small foam sample was ramped at 20 °C/min from room temperature to 550 °C at ambient pressure. Fig. 6E and F shows predicted and measurements [5] for an *isothermal TGA experiment* where the temperature of a small foam sample was ramped at 20°/min from room temperature to 400 °C and held for 2 h at ambient pressure, respectively. A temperature of 400 °C was high enough for all four of the SREF reaction steps to be significant.

In Fig. 6A and E, the measured solid fraction, S_f, is plotted as open circles and the mean solid fraction prediction is plotted as a black line. The 95% prediction interval is plotted as dashed lines and represents the mean solid fraction plus or minus two standard deviations. The gas generation rates are plotted in Fig. 6B and F. The units on the gas generation rates are s^{-1}. By multiplying by the sample mass, the gas mass generation rate (g/s) can be obtained. The rate of gas species evolution shows which species are prevalent as the reaction progresses. The overall rate of gas evolution is consistent with the measurements as discussed in Ref. [6].

Table 2
SREF model parameters[a]

A_1	1×10^{13} s^{-1}	$\gamma_{i,0}$	1
A_2	2×10^{15} s^{-1}	$(d^*/\theta)_i$	1
A_3	2×10^{16} s^{-1}	$\rho_{f,0}$	0.312 g/cm^3
A_4	6×10^{12} s^{-1}	$\rho_{p,0}$	1.09 g/cm^3
E_1	28.7 ± 1 kcal/mol	σ_{E1}	0.76 kcal/mol
E_2	46.4 ± 1 kcal/mol	σ_{E2}	2.8 kcal/mol
E_3	58.1 ± 1 kcal/mol	σ_{E3}	6.6 kcal/mol
E_4	43.5 ± 1 kcal/mol	σ_{E4}	0.79 kcal/mol

[a] Uncertainty is only considered for the activation energies where ±1 kcal/mol represents one standard deviation.

The four SREF populations, S, L_1, L_2, and L_3, and the bridge population, p, are plotted in Fig. 6C for the ramped experiment. The populations are similar for the isothermal experiment. The most prevalent reaction from room temperature to about 200 °C is reaction 1 that describes desorption of the "sorbed" species. Consequently the most important parameter in this region that affects uncertainty in the prediction is the activation energy for reaction 1 as shown in Fig. 6D. The second reaction, responsible for OS evolution, is prominent between 200 and 300 °C. The reaction responsible for the mixed-product (MP) species is significant from about 200 °C to the end of the reaction. The fourth reaction, which is responsible for BPA evolution, is prevalent between 250 and 500 °C. The root mean squared (RMS) errors for the solid fraction predictions in Fig. 6A and E were 1.8 and 1.0%, respectively.

Fig. 7A and B shows the effects of heating rate on the calculated solid fraction and the gas generation rate, respectively. In Fig. 7A, the calculated solid fraction profile shifts to higher temperatures with increasing heating rates as observed experimentally by Clayton [5]. The magnitude that each curve shifts to higher temperature is related to the reaction rates. Thermal decomposition is a temperature-dependent kinetic process. If the reaction rates were faster, the profiles depicted in Fig. 7A would be grouped closer together. If the reaction rates were slower the separation between the profiles would be farther apart.

The effects of pressure on decomposition are shown in Fig. 7C for a constant sample heating rate of 20 °C/min and the default diffusion resistance ($d^*/\theta = 1$ cm). The effect of elevated pressure is similar to the effects of confinement at ambient pressure shown by Erickson et al. [6] in that the TGA profiles shift to higher temperatures. Pressure affects gas evolution rates by both the VLE model and the diffusion model since the separation factor or K-value [see Eq. (17)] and the BAS diffusivity [see Eq. (8)] are inversely proportional to pressure. Fig. 7D shows the effects of pressure on predicted solid fraction for a constant sample heating rate of 20 °C/min with the diffusion resistance an order of magnitude higher than the default value ($d^*/\theta = 10$ cm). The VLE model is the same for predictions in both Fig. 7C and D, and differences in the predicted profiles are attributed solely to increased diffusion resistance.

Recall that d^*/θ represents the characteristic diffusion length divided by a tortuosity-like term. An increase in d^*/θ is equivalent to an increase in the diffusion resistance, which causes the decomposition profiles to shift to higher temperatures. Increasing the diffusive resistance artificially decreases the driving potential or concentration differences between species at the reaction sites and in the bulk gas. An increase in

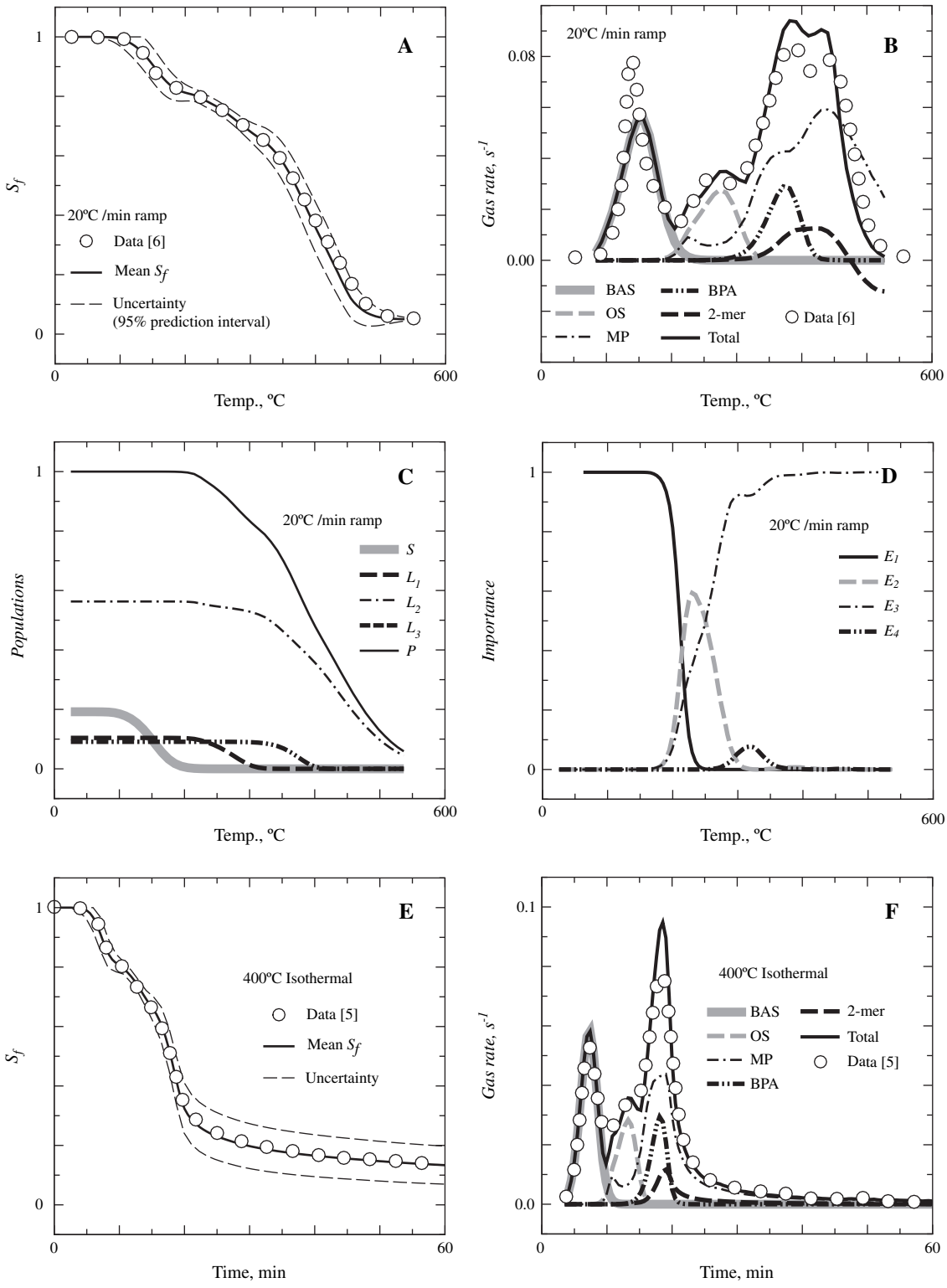

Fig. 6. Various predictions (lines) and measurements [5,6] (open circles) of TGA samples heated at 20 °C/min at two separate laboratories: (A) solid fraction, (B) gas production rate, (C) populations, (D) importance factors, (E) solid fraction (isothermal), and (F) gas production rate (isothermal). The sample in E and F was ramped at 20 °C/min from room temperature to 400 °C and then held at 400 °C.

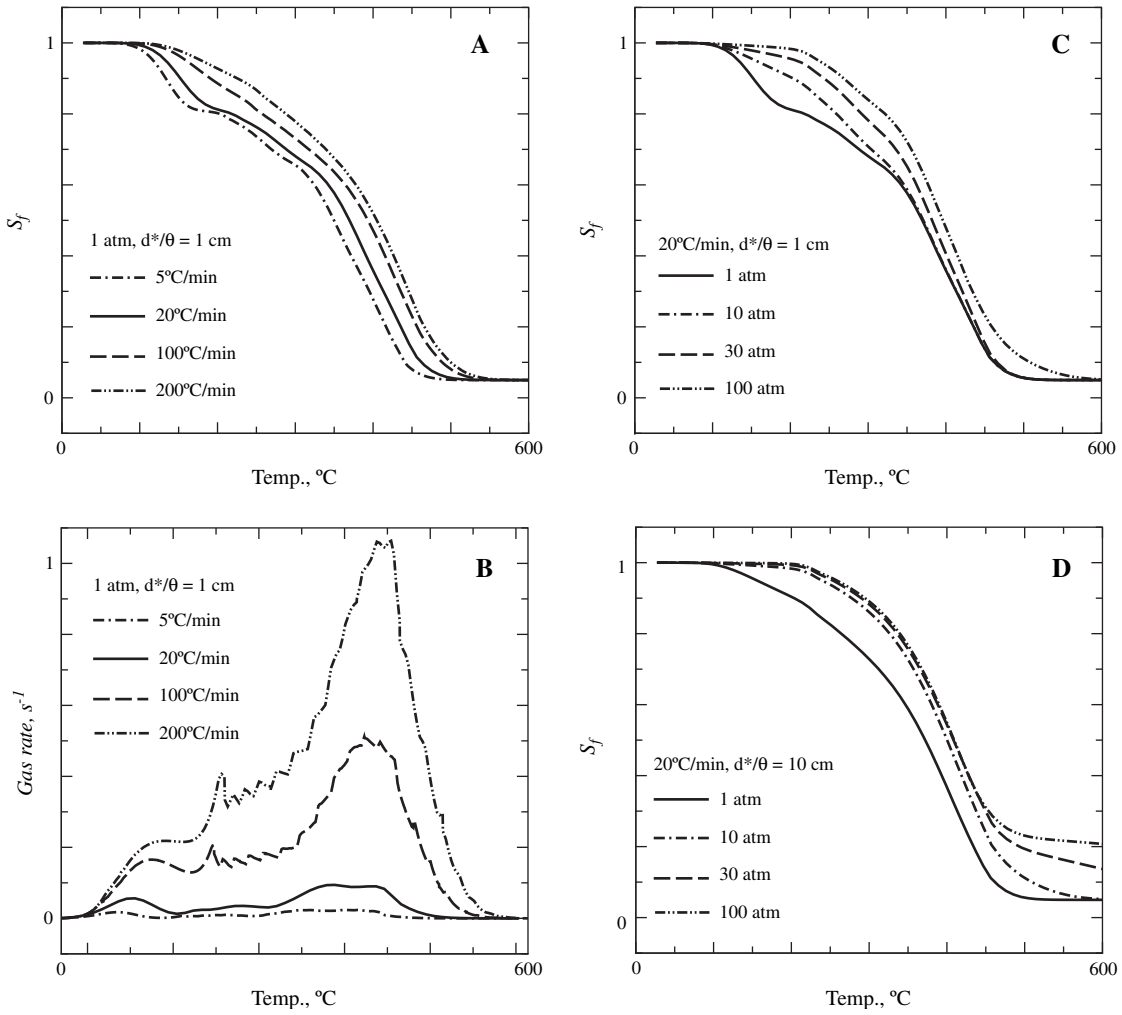

Fig. 7. Predicted effect of sample heating rate on (A) solid fraction and (B) gas evolution rates. Predicted effect of pressure on solid fraction using (C) the default diffusion resistance ($d^*/\theta = 1$ cm) and (D) 10 times the default diffusion resistance ($d^*/\theta = 10$ cm).

diffusive resistance is expected when decomposition products are "confined locally." The true driving potential does not decrease by a fixed amount, but decreases gradually as the bulk concentrations change with reaction. The blowing agent and surfactant is affected the most by the increase in mass transport resistance and remains in the residue, even at 600 °C as shown in Fig. 7D. More surfactant in residues obtained from high-pressure decomposition should contain more silicon than residues obtained from low-pressure decomposition since the surfactant is composed of more than 70% by mass of silicon.

8.2. Constant volume hot cell

The hot cell experiment shown in Fig. 8A was designed to characterize energetic materials [25] and polymeric foams [26] using a pneumatic cylinder controlled by a displacement gauge. Renlund [27] used the load cell to maintain a constant volume decomposition chamber by confining the ends of a cylindrical foam sample between two pistons with the lateral surface of the foam being confined by a solid cylinder of stainless steel. Decomposition gases caused the pressure within the constant volume chamber to increase, which required a larger load to maintain the constant volume decomposition chamber. The pressure was inferred by dividing the measured load by the cross sectional area of the pistons. Displacement, foam temperature, and chamber pressure measured by Renlund [27] is given in Fig. 8B. Various states of the foam and confining chamber are given in Table 3 with additional parameters given in Table 4.

Fig. 8B shows the absolute value of the measured foam displacement as Δh, which refers to the change in height of the foam sample in cm. In Fig. 8B, the measured displacement has three states marked 1, 2, and 3, which represent the state of the sample before the initial preload displacement, after the initial preload displacement, and at the end of the experiment, respectively. The preload displacement causes the sample to distort by shortening the height of the sample

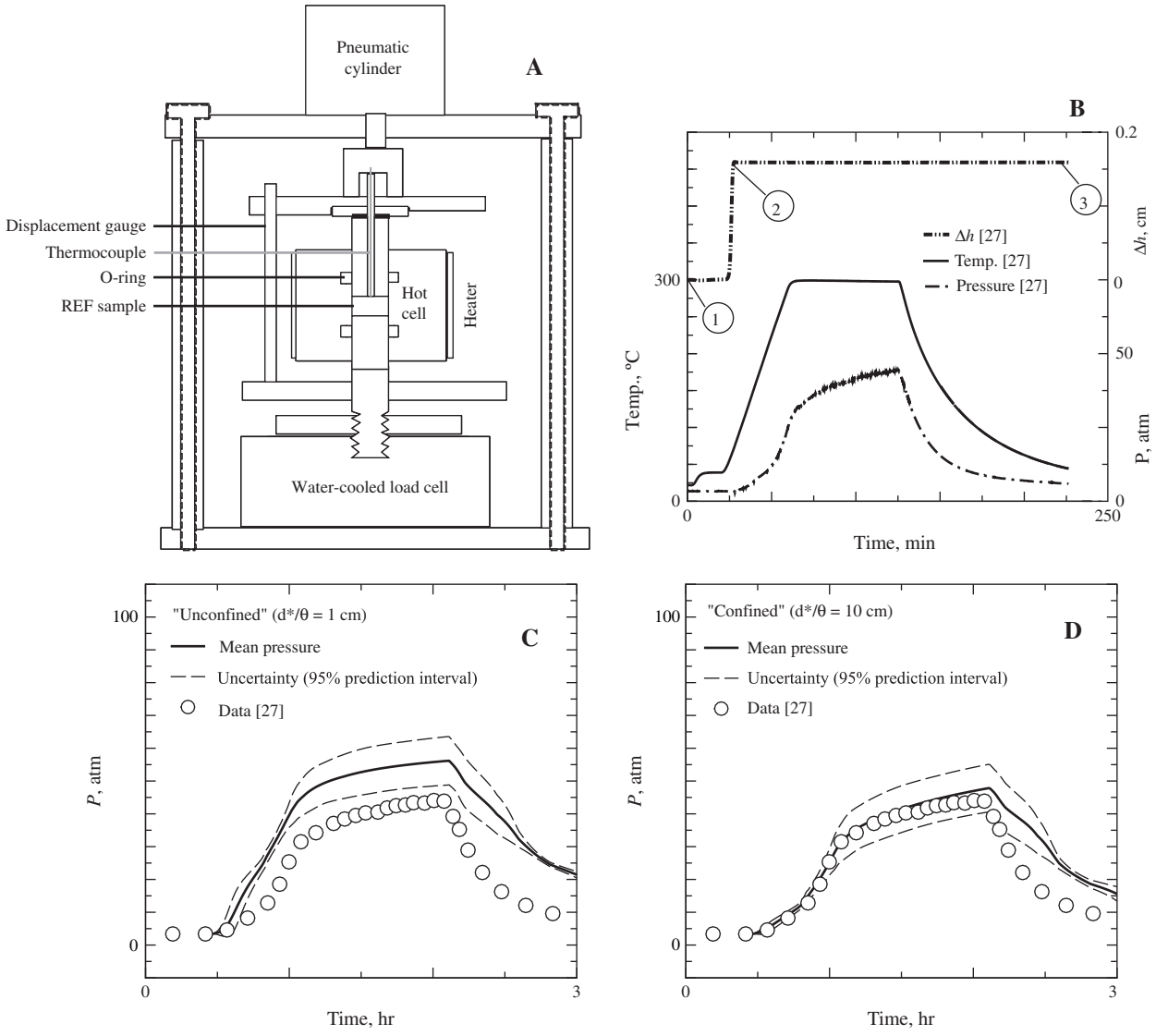

Fig. 8. (A) Schematic of hot cell apparatus. (B) Foam sample displacement, temperature, and pressure measured by Renlund [27]. 1, 2, and 3 in B represent the sample state before initial preload displacement, after initial preload displacement, and at the end of the experiment, respectively (see Table 3). (C) Predicted pressure using default diffusion resistance expected when products are "not confined locally" ($d^*/\theta = 1$ cm). (D) Predicted pressure using 10 times the default diffusion resistance ($d^*/\theta = 10$ cm) showing better agreement with pressure measured by Renlund [27]. Increasing the diffusive resistance is equivalent to artificially decreasing the driving potential or concentration differences between species at the reaction sites and in the bulk gas. An increase in diffusive resistance is expected when decomposition products are "confined locally."

and increasing the diameter of the cylindrical sample. These three states are described in Table 3. The sample deformed at the glass transition temperature with an initial load of 3.39 atm. The density of the foam at point 2, after being deformed, was 0.312 g/cm^3 as given in Table 3. From point 2 onward, the decomposition chamber volume was controlled by the displacement gauge and set to be constant with a height of 0.504 cm and a diameter of 1.27 cm.

Fig. 8C and D shows a comparison between the predicted pressure (lines) and the pressure inferred from the load cell signal (symbols) using a mean value analysis for uncertainty with the default diffusion resistance ($d^*/\theta = 1$ cm) and for 10 times the diffusion resistance ($d^*/\theta = 10$ cm), respectively. The percent error between the mean predicted pressure (56 atm) and measured pressure (44 atm) at 2 h was 27% with the default diffusion resistance ($d^*/\theta = 1$ cm). Much better results were obtained when the diffusion resistance was increased by a factor of 10 ($d^*/\theta = 10$ cm), where the predicted pressure at 2 h was 47 atm giving an error of 7%. The largest error occurs in the unloading region after 125 min when the temperature drops considerably.

Local confinement of decomposition products causes the driving potential for diffusion to drop since the concentration differences between the species at the

Table 3
Three foam states in hot cell experiment shown in Fig. 8(B) [27]

Description	(1) Before preload	(2) After preload	(3) Postmortem
Foam mass	0.1993 g	0.1993 g	0.131 g
Solid fraction	1	1	0.657
Height of chamber	0.663 cm	0.504 cm	0.504 cm
Diameter of chamber	1.27 cm	1.27 cm	1.27 cm
Height of foam	0.663 cm	0.504 cm	0.095 cm
Diameter of foam	1.257 cm	1.27 cm	1.27 cm
Volume of foam	0.823 cm^3	0.638 cm^3	0.120 cm^3
Density of foam	0.242 g/cm^3	0.312 g/cm^3	1.09 g/cm^3

reaction sites and the concentration in the bulk gas is smaller than when the decomposition gases are swept from the system. The larger resistance is analogous to a confinement effect and the difference between the results in Fig. 8C and D is assumed to be caused by confining the decomposition gases. The larger error during the unloading phase of the experiments was attributed to neglecting reverse reactions in the SREF model. The temperature of the sample at 140 min is 200 °C as shown and drops to 100 °C at 170 min. The Diels–Alder reaction may be significant at these cooler temperatures.

9. Large-scale predictions

Erickson et al. [6] describe component-scale radiant heat experiments of stainless steel cylindrical containers filled with REF200 encapsulant and exposed to fire-like heat fluxes. A postmortem radiograph of the residue left in one of the fully-confined radiant heat experiments [6] showed a complicated structure composed of thin layers of partially decomposed foam (residue) separated by large void regions. The component-scale experiments were simulated with some success by using a dynamic radiation enclosure filled with nonparticipating gases [28]. The change in the enclosure geometry was defined by the evolving reacted solid fraction based on the SREF chemistry model.

Fig. 9A shows the configuration of one of the radiant heat experiments with the top of the cylinder quickly ramped (220 °C/min) from room temperature to 900 °C and held for about 4 min until the confinement ruptured. Thermocouple locations are marked in Fig. 9A with H, 1, 2, 3, and C. The H-thermocouple refers to the "hot" side of the can that was exposed to quartz heating lamps. The boundary temperatures for the model are shown in Fig. 9B. The top and bottom of the can were set to the values of the H- and C-thermocouple. The side of the can was specified using thermocouples 1, 2, and 3 using linear interpolation. The bulk density of the REF200 foam was 0.128 g/cm^3.

Table 4
Pressurization parameters for the hot cell [27]

Description	Value
Initial pressure	3.39 atm
Initial temperature	71 °C
Initial foam density	0.312 g/cm^3
Initial polymer density	1.09 g/cm^3
Element volume	0.638 cm^3
Initial gas volume	0.455 cm^3
Initial gas moles	5.46×10^{-5} mol

Fig. 9C shows three radiographs from Ref. [6] with the front highlighted by arrows. At 4 min, the linear front is near the heated surface located at the top of the can. The front becomes nonlinear as it moves down to the middle of the can as shown in Fig. 9C at 5 min. At 5 min, the front has become three-dimensional and the front shape is difficult to estimate with the radiographs. Fig. 9C also shows predictions of the front using the default diffusion resistance associated with "unconfined" decomposition ($d^*/\theta = 1$ cm) and "confined" decomposition ($d^*/\theta = 10$ cm). The predicted front locations, highlighted with white arrows in Fig. 9C using $d^*/\theta = 1$ cm and $d^*/\theta = 10$ cm, are essentially the same. The predicted foam densities are slightly different at 6 min, e.g. $\rho_f = 0.17$ g/cm^3 when $d^*/\theta = 1$ cm and $\rho_f = 0.16$ g/cm^3 when $d^*/\theta = 10$ cm. The radiographs indicate that the front is not well defined and liquids may be present between 5 and 6 min. The foam may also strain due to thermal expansion and pressure loads, which are beyond the scope of the current paper. A stress–strain relationship (constitutive model) for reactive materials is needed to describe these coupled thermal, chemical, and mechanical phenomena. Nevertheless, the pressure increase due to decomposition may be approximated with the thermal/chemical SREF model as shown in Fig. 9D.

Fig. 9D shows a comparison between the measured and predicted pressure for the radiant heat experiment. The deformation of the container caused by thermal expansion and pressure loading was not modeled. However, the chemistry model is pressure dependent and feedback between the chemistry mechanism and pressurization was included as shown in Fig. 1. In Fig. 9D, pressure was predicted with the default diffusion parameters ($d^*/\theta = 1$ cm) and with the diffusion resistance increased by an order of magnitude ($d^*/\theta = 10$ cm). For the most part, the two predicted pressure profiles span the transducer response. However, the pressure transducer response between 4 and 6 min fall below both predictions, where the radiographs show the development of a three-dimensional regression front, and thermocouples 2 and 3 indicate a jump in temperature between 4 and 6 min. Channeling of decomposition products along the confinement container walls would explain these events and give a plausible explanation of the disagreement between the predicted pressure and transducer response between 4 and 6 min.

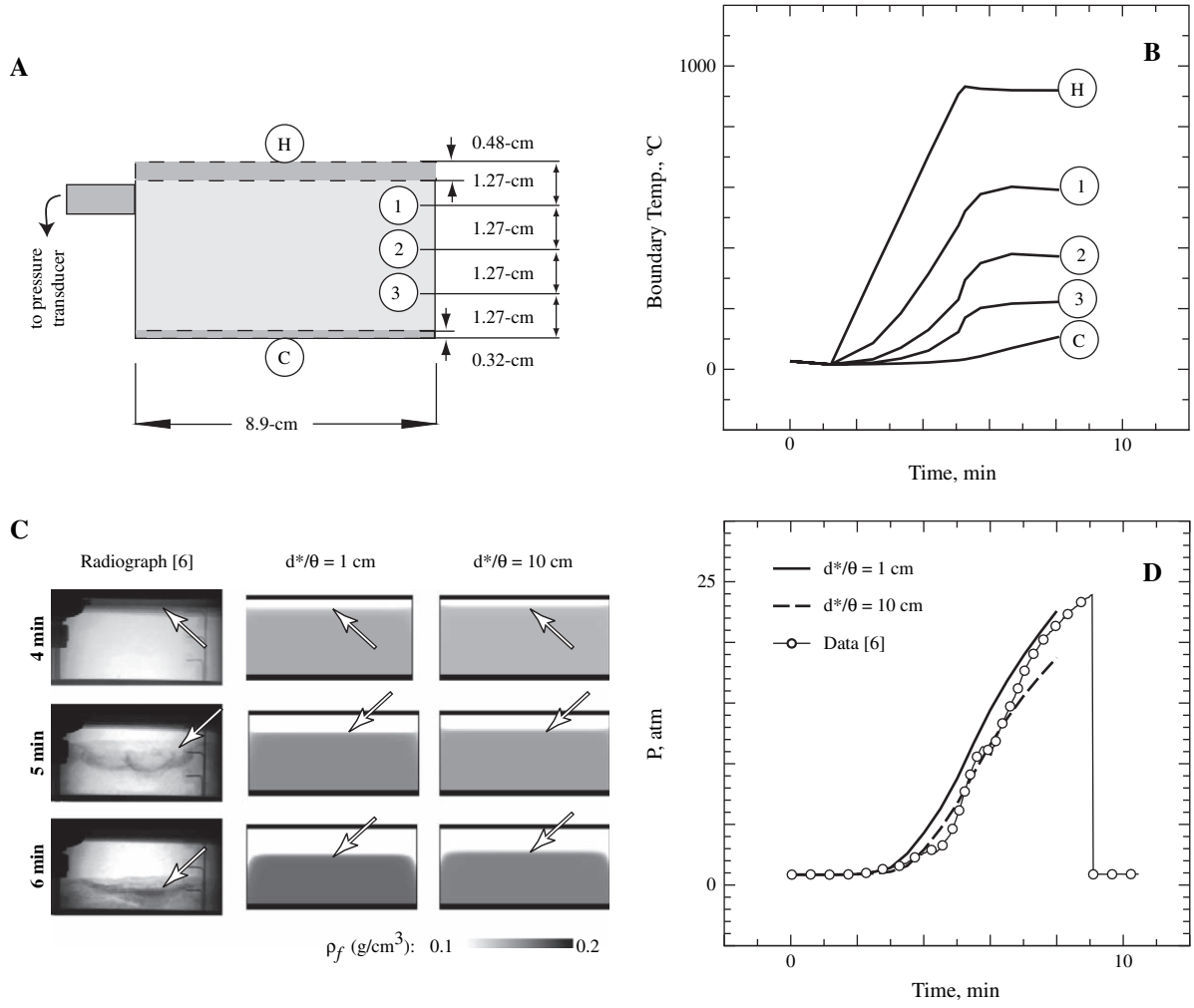

Fig. 9. (A) Schematic drawing, (B) boundary temperatures, (C) measured [6] and predicted front locations and (D) measured [6] and predicted pressures for large-scale foam experiment. The locations of the thermocouples are given by H, 1, 2, 3, and C. The measured front locations can be seen as density variations in the radiographs.

10. Summary and conclusions

A semi-empirical model based on the chemical structure of rigid, closed-cell removable epoxy foam composed of various gases absorbed on to an epoxy polymer has been presented. The model uses one reaction to describe desorption of gases from the polymer, three reactions to describe thermal degradation of an epoxy polymer, and neglects reversible reactions. The reaction rates were distributed normally based on the extent of reaction. Mass transport effects were included by assuming that diffusion rates are proportional to species concentration differences between the reaction sites and the bulk gas. The model uses lattice statistics to resolve polymer fragment distributions and vapor–liquid equilibrium with pressure-dependent activity coefficients to determine the vapor–liquid split. Pressure and density were determined by assuming zero thermal or mechanical strain in the condensed-phase and negligible flow resistance in the gas-phase.

The model lattice was composed of sites connected by octamethylcylotetrasiloxane (OS) bridges, mixed-product (MP) bridges, and bisphenol A (BPA) bridges. The mixed products were treated as a single species, but are likely composed of phenols, cresols, and furan-type products. The model considers 10 species that can be separated into two categories – (1) seven VLE species and (2) three non-VLE species. The VLE species can reside in either the condensed-phase, the gas-phase, or in both phases as determined using a vapor–liquid equilibrium model using pressure-dependent activity coefficients. The non-VLE species always remain in the condensed-phase. The VLE species include BAS, OS, MP, BPA, 2-mers, 3-mers, and 4-mers, representing the blowing agent and surfactant as a single species, octamethylcylotetrasiloxane, mixed products, bisphenol A, and polymer fragments that contain two, three, or four sites, respectively. The three non-VLE species have large molecular weights with low vapor pressures. These species include NV-residue, *L*-mers, and XL-mers;

representing nonvolatile residue, residue composed of polymer fragments from 5-mers to 10-mers, and residue composed of 11-mers to ∞-mer. The molecular weights of the NV-residue and XL-mer residue were specified.

The SREF model was evaluated with TGA data taken at two separate laboratories [5,6]. The first simulation was a *ramped* TGA experiment that considered a small sample (0.005 g) ramped from room temperature to 550 °C, and the second simulation was of an *isothermal* TGA experiment that considered a small sample quickly ramped (20 °C/min) to 400 °C and held. The RMS errors for the solid fraction predictions when compared to measurements for the ramped and isothermal experiments were 1.8 and 1.0%, respectively. Mean value analysis was used to show the relative importance of model parameters. The kinetic parameters dominated the calculated uncertainties. Effects of heating rate and pressure were presented. Mass loss profiles shifted to higher temperatures when either heating rate or pressure was increased systematically. The effect of confinement was addressed semi-empirically by increasing the diffusion resistance by an order of magnitude. The effect of confining the decomposition gases is to shift mass loss profiles to higher temperatures, which has also been observed by Erickson et al. [6].

The ability of the SREF model to extrapolate from predicting mass loss in unconfined TGA experiments to predicting pressurization in a fully-confined constant volume hot cell experiment [25–27] was demonstrated. In the hot cell experiment, a cylindrical foam sample (0.2 g) was heated to 300 °C with pressure inferred from a load cell response. One simulation was performed with the same diffusion resistance used in the "unconfined" TGA simulations, and another simulation was performed with the diffusion resistance increased by an order of magnitude to mimic "confinement" effects. The simulation with the "unconfined" diffusion resistance predicted the pressure to be 27% higher than the inferred pressure after 2 h of heating. The predicted pressure was only 7% higher than the inferred pressure when the diffusion resistance was increased by an order of magnitude. These simulations suggest that unconfined decomposition (decomposition gases swept from the system) is not the same as confined decomposition (decomposition gases kept within the system). Difference between measured and predicted pressure may also be related to uncertainty in the sample temperature, complex phase equilibrium during condensation, reversible reactions not considered in the model such as the Diels–Alder reaction. More accurate results could have been obtained at substantial complexity by including reversibility in the reaction mechanism.

The ability of the SREF model to extrapolate from small-scale experiments, such as the TGA and hot cell experiments, to large-scale experiments was demonstrated by simulating the pressure rise in an 8.9 cm diameter by 4.28 cm tall cylinder filled with 34 g of REF200 foam exposed to fire-like heat fluxes. One simulation was performed with the same diffusion resistance used in the "unconfined" TGA simulations, and another simulation was performed with the diffusion resistance increased by an order of magnitude to mimic "confinement" effects. After 8 min of heating, the predicted pressure with unconfined diffusive resistance (19 atm) and predicted pressure approximating confined diffusive resistance (22 atm) were within experimental uncertainty of the transducer response (21 atm). The predicted fronts at late times were smooth and one-dimensional. However, the fronts in the radiographs [6] were dark and irregular, and temperature jumps measured on the container sides implied channeling of hot decomposition products.

The SREF decomposition model has been shown to: (1) predict mass loss within 1–2% of measured values from small epoxy foams samples (0.005 g) heated in several *unconfined* TGA experiments, (2) predict pressure within 7–27% of pressure implied from load cell measurements in a *fully-confined* constant volume hot cell experiment containing a larger foam sample (0.2 g), and (3) predict pressure within 5–10% of the pressure transducer response in an even larger fully-confined foam sample (34 g) exposed to temperatures as high as 900 °C. The SREF model has been successful in simulating a variety of different experiments from different laboratories with foam sample size varying from 3–4 orders of magnitude. Despite the success of the model, several modeling deficiencies should be addressed for more accurate and insightful predictions. The effect of confinement needs to be addressed by considering the change in bulk gas concentration due to flow in and flow out of systems of interest. A reactive elastic/viscoplastic constitutive stress–strain model should be considered for the foam as well as thermal expansion and elastic response of the confining container. Better activity coefficient, diffusivity, and thermophysical property models and data are also needed. In other words, a more detailed coupled-physics modeling approach (thermal, chemical, mechanical, flow, etc.) of both the gas- and condensed-phases is needed to more fully understand polymeric foam response during exposure to abnormal thermal environments such as fire.

Acknowledgements

Many colleagues have contributed data, technical advice, and management assistance regarding foam response modeling. I am grateful to all of them and apologize if I have inadvertently failed to acknowledge them in print. These colleagues include Terry Aselage, Jim Aubert, Jeremy Barney, John Bentz, Ben Belone, Ted Borek, Steve Bova, Jo Bridge, Jaime Castañeda, Tze Y. Chu, Dan Clayton, David Darrow, Dean

Dobranich, Kevin Dowding, Ken Erickson, Tom Fletcher, Nick Francis, Walt Gill, Kevin Grossarth, Chuck Hanks, Mike Hassard, Gene Hertel, David Ho, Roy Hogan, Paige Jackson, Robert Kerr, Andy Kraynik, Marvin Larsen, Shawna Liff, Steve Lott, Jill Miller, Jim Nakos, Mike Neilsen, John Oelfke, Jack Pantuso, Martin Pilch, Mike Prairie, Mike Ramirez, Art Ratzel, Anita Renlund, Ed Russick, Brian Rutherford, Thomás Sánchez, Jerry Stoker, Amy Sun, Kyle Thompson, Paul Thompson, Steve Trujillo, Scot Waye, and Steve Younghouse.

References

[1] Loy DA, Wheeler DR, Russick EM, McElhanon JR, Saunders RS. Method of making thermally removable epoxies. Patent #6,337,384, Sandia National Laboratories; January 2002.
[2] Aubert JH, McElhanon JR, Saunders RS, Sawyer PS, Wheeler DR, Russick EM, et al. Progress in developing removable foams, adhesives, and conformal coatings for the encapsulation of weapon components. Sandia National Laboratories report SAND2001-0295. Albuquerque; 2001.
[3] McElhanon JR, Russick EM, Wheeler DR, Loy DA, Aubert JH. Removable foams based on an epoxy resin incorporating reversible Diels–Alder adducts. J Appl Polym Sci 2002;85(7): 1496–502.
[4] Hobbs ML. SREF—a simple removable epoxy foam decomposition chemistry model. Sandia National Laboratories report SAND2003-4550. Albuquerque; 2003.
[5] Clayton DJ. Modeling flow effects during polymer decomposition using percolation lattice statistics. Dissertation, Brigham Young University, Provo; 2002.
[6] Erickson KL, Trujillo SM, Thompson KR, Sun AC, Hobbs ML, Dowding KJ. Liquefaction and flow behavior of a thermally decomposing removable epoxy foam. In: Mammoli AA, Brebbia CA, editors. Computational methods in materials characterisation. Southampton: WIT Press; 2004. p. 217.
[7] Hobbs ML. Finite element modeling of syntactic foam. North American Thermal Analysis Society, 32nd meeting in Williamsburg, VA; 2004. J Therm Anal Cal, in press.
[8] Pitt GJ. The kinetics of the evolution of volatile products from coal. Fuel 1962;41:267–74.
[9] Laurendeau NM. Heterogeneous kinetics of coal char gasification and combustion. Prog Energy Combust Sci 1978;4:221.
[10] Froment GF, Bischoff KB. Chemical reactor analysis and design. 2nd ed. New York: John Wiley & Sons, Inc; 1990.
[11] Bird RB, Stewart WE, Lightfoot EN. Transport phenomena. 2nd ed. New York: John Wiley & Sons, Inc; 2002.
[12] Hobbs ML, Erickson KL, Chu TY. Modeling decomposition of unconfined rigid polyurethane foam. Polym Degrad Stab 2000;69:47–66.
[13] Grant DM, Pugmire RJ, Fletcher TH, Kerstein AR. Chemical model of coal devolatilization using percolation lattice statistics. Energy Fuels 1989;3:175.
[14] Fletcher TH, Kerstein AR, Pugmire RJ, Solum MS, Grant DM. Chemical percolation model for devolatilization 3. Direct use of ^{13}C NMR data to predict effects of coal type. Energy Fuels 1990;4:54.
[15] Henley EG, Seader JD. Equilibrium-stage separation operations in chemical engineering. New York: John Wiley & Sons Inc; 1981.
[16] Daubert TE, Danner RP, Subul HM, Stebbins CC. Physical and thermodynamic properties of pure compounds: data compilations, extant 1994. Bristol, PA: Taylor & Francis; 1994.
[17] Paolucci S. On the filtering of sound from the Navier–Stokes approximation. Sandia National Laboratories report SAND82-8257, Livermore, CA; 1982.
[18] Erickson KL. DSC data. Personal communication to ML Hobbs; January 15, 2003.
[19] Glicksman LR. Heat transfer in foams. In: Hilyard A, Cunningham NC, editors. Low density cellular plastics physical basis of behavior. London: Chapman & Hall; 1994. p. 104 [chapter 5].
[20] Collishaw PG, Evans JRG. Review—an assessment of expressions for the apparent thermal conductivity of cellular materials. J Mater Sci 1994;29:226.
[21] Dobranich D, Gill WA. Thermal model validation test unit for the W76-1 AF&F—design, experiments, and simulations. Sandia National Laboratories report SAND2002-1769, Albuquerque, NM; 2002.
[22] Aselage TL. C_p measurements for removable epoxy foam. Personal communication to ML Hobbs; September 18, 2001.
[23] Gembarovic J, Taylor RE. Thermophysical properties of plastic sample—a report to Sandia National Laboratories. Thermophysical Properties Research Laboratory, Inc. report TPRL2868, West Lafayette, IN; October 2003.
[24] Hobbs ML, Romero VJ. Uncertainty analysis of decomposing polyurethane foam. Thermochim Acta 2002;384:393.
[25] Renlund AM, Miller JC, Trott WM, Erickson KL, Hobbs ML, Schmitt RG, et al. Characterization of thermally degraded energetic materials. Eleventh international detonation symposium. Snowmass, CO; 1998.
[26] Ulibarri TA, Derzon DK, Erickson KL, Castaneda J, Borek TT, Renlund AM, et al. Preliminary investigation of the thermal decomposition of ablefoam and EF-AR20 foam (Ablefoam Replacement). Sandia National Laboratories report SAND2002-0183. Albuquerque; 2002.
[27] Renlund AM. Hot cell data for REF encapsulant. Personal communication to ML Hobbs; November 11, 2002.
[28] Hobbs ML. Response of removable epoxy foam exposed to fire using an element death model. Sandia National Laboratories report SAND2004-4320. Albuquerque; 2004.